Research Article

Nehad Ali Shah, Areej Abdullah Alabduljabbar, Zeeshan, and Se-Jin Yook*

Thermal and stability analysis of silver–water nanofluid flow over unsteady stretching sheet under the influence of heat generation/ absorption at the boundary

https://doi.org/10.1515/ntrev-2025-0178
received December 18, 2024; accepted May 12, 2025

Abstract: The aim of this study is to examine a numerical analysis of nanofluid (NF) containing silver (Ag) nanoparticles using water (H_2O) as a host fluid through an unsteady stretching sheet with stability analysis. The thermal performance of the NF is also examined in the present study, which has a significant role in aerodynamics and space sciences. A mathematical framework is created for the Ag nanofluids in terms of partial differential equations (PDEs). Through resemblance variables, the system of PDEs is made dimensionalized in terms of ordinary differential equations and then computed by a boundary-value problem fourth-order algorithm. The impacts of the physical aspects on the flow features are reported *via* graphs and tables. The findings show that multiple branches occur due to suction and injection. For the confirmation of the stable solution, stability examination is executed and confirms that the first branch is stable. It is reported that both NFs have high thermal efficiency; however, Ag–H_2O represents significant thermal efficiencies. The present study is compared with available analyses to confirm the analysis under limited assumptions.

Keywords: silver–water (Ag–H_2O) nanofluid, multiple solutions, numerical solutions, suction/injection

*** Corresponding author: Se-Jin Yook,** School of Mechanical Engineering, Hanyang University, 222 Wangsimni-ro, Seongdong-gu, Seoul, 04763, Republic of Korea, e-mail: ysjnuri@hanyang.ac.kr
Nehad Ali Shah: Department of Mechanical Engineering, Sejong University, Seoul, 05006, Republic of Korea,
e-mail: nehadali199@sejong.ac.kr
Areej Abdullah Alabduljabbar: Department of Mathematics, College of Sciences, King Saud University, P.O.Box 2455, Riyadh, 11451, Saudi Arabia,
e-mail: arabduljabar@ksu.edu.sa
Zeeshan: Department of Mathematics and Statistics, Bacha Khan University Charsadda, Charsadda, KP, Pakistan,
e-mail: zeeshan@bkuc.edu.pk

Nomenclature

$A_1 = \gamma l u_0^{-1}$	unsteadiness number
f_w	suction/injection parameter
k_{nf}	thermal conductivity of nanofluid
ρ_{nf}	density of nanofluid (kg m^{-3})
HT	heat transfer
NF	nanofluid
F	dimensionless velocity
$\mathrm{Pr} = \frac{v_f}{k_f}$	Prandtl number
T	temperature (T)
$(\rho C_{\mathrm{p}})_{\mathrm{nf}}$	heat capacity of nanofluid (W m^{-1} K^{-1})
μ_{nf}	viscosity of nanofluid (m^2 s^{-1})
u, v	velocities components (m s^{-1})
η	similarity variable
θ	dimensionless temperature
ϕ	volume friction

1 Introduction

The thermal efficiency of fluids holds critical significance within the aerospace and industrial domains. Numerous engineering and mechanical operations necessitate a considerable degree of heat transfer (HT) in order to be executed effectively. The traditional liquids are unable to provide the necessary heat to complete the operation. The flow and HT capabilities of the host liquid can be increased by suspending nanomaterials in the base fluid. These fluids have highly developed HT properties that pave the way for engineers and industrialists in the current world. The study of aerodynamics, medical research, chips used in computers, paint manufacturing, the production of aircraft parts, and many more fields are among the potential uses of nanofluids (NFs). Elgazery [1] inspected the non-uniform heat generation and absorption of a porous stretched sheet containing NF. The impact of magnetic fields was also

investigated in his study. Nasir *et al.* [2] portrayed the thin-film flow of NF in the porous medium to analyses the heat rate using a time-dependent starching sheet. Using the Taguchi-GRA approach, Raza and Ashfaq [3] examined how to optimize HT in two-phased NF flow across a biaxial sheet. The improvement of the HT rate of a trihybrid NF inserted inside two parallel coaxial tubes using RSM was investigated by Raza *et al.* [4]. Utilizing a ferromagnetic tetra-hybrid NF, Shutaywi *et al.* [5] investigated the optimization of heat transport in a channel with extending walls. The improvement of the flow rate of a radiated micropolar NF with sensitivity evaluation was examined by Alahmadi *et al.* [6]. Bhattacharyya *et al.* [7] reported magnetized NF heat transmission across a stretched sheet. The numerical consequences were obtained using the RK4 method. It was revealed that HT increased due to the Brownian motion.

The fluid behavior over the stretched sheet was scrutinized by Mansur and Ishak [8]. A numerical solution has been obtained through the RK4 approach, and the results for the emerging factors are obtained through graphs. It was revealed that there is a direct relationship between the heating surface and HT, while the HT declines as the unsteady flow factor is enhanced. Dutta and Roy [9] described the heat flux features of the magnetohydrodynamics (MHD) movement flowing over an elongating surface. Certain assumptions have been considered to model the flow problem and show the outcomes for the stream phenomena. The work is quite interesting, but it absences novelty regarding HT in the NF from a physics point of view, such as chemical processes, thermal radiation, and magnetic fields. The dynamic of viscous fluid flow with HT through an extended surface was described by Cortell [10]. He reported the problem for two different phases: prescribed and uniform sheet temperature. The results were displayed through graphs for each phase. He examined the work only for the host fluid. Furthermore, this work could be extended to numerous NFs models regarding multiple flow geometries. An advanced HT study of 3D MHD NF flow across an expanding sheet including thermal energy and heat sources was studied by Afzal and Kamran [11]. In the study of fluid analysis, viscous dissipation plays a significant role in altering its characteristics. Mahabaleshwar *et al.* [12] investigated the influence of radiation in laminar flow using a ternary NF *via* a stretching sheet. Similarly, Mahabaleshwar *et al.* [13] examined two NF with a viscosity ratio *via* an accelerated plate. Three-dimensional MHD NF flow over an extended sheet featuring thermal and a heat sink was studied by Kamran *et al.* [14].

It is well established that the host fluid (the base fluid) has low thermal conductivity and is not a worthy conductor. So, it is necessary to explore the HT mechanism through a time-dependent stretching and contracting sheet. Such a framework has sufficient applications in industrial and mechanical engineering. There is limited investigation into HT *via* unsteady stretching or shrinking sheets using NFs. The NF containing silver nanoparticles ($Ag–H_2O$) has significant advantages over host fluids regarding its transportation. The implications of bioconvection cross propagation on MHD movement of NFs over three distinct geometries involving melting were examined by Kamran *et al.* [15]. The magnetized bioconvection movement of Jeffrey NF containing motile bacteria over a stretched sheet was studied by Waqas *et al.* [16].

Since numerous investigators have found non-unique results in the majority of the studies, the evaluation of stability is crucial to getting a stable solution. The stability investigation in mixed convection flow across a transparent channel was first applied by Merkin [17]. Weidman *et al.* [18] subsequently utilized this idea to study a flow issue across a rotating plate utilizing stability analysis. The stagnation boundary movement across a porous upward sheet was then investigated by Merrill *et al.* [19]. Harris *et al.* [20] added the slip impact to the Merrill *et al.* [19] suggested model by utilizing the Brinkman flow theory. The interaction between stability and duality in magneto-radiated Casson NF flow across a stretched cylinder was examined by Deebani *et al.* [21]. The consequences of slip on MHD hybrid ferrofluid movement having acute magnetic attraction on a stretching sheet were investigated by Asghar *et al.* [22]. The hybrid NF dynamics on an exponentially contracting/extending Riga sheet during radiative heat flow were computationally investigated by Yashkun *et al.* [23]. The multiple solutions of MHD radiative movement of Casson NF across a contracting/extending cylinder were studied by Soomro *et al.* [24]. They deduced that the second solution is unstable while the first is reliable (stable).

A thorough survey of the present literature indicates that multiple research projects have been executed to investigate the thermal properties of base liquids that do not utilize advanced thermal enhancement, particularly in water solutions with Ag nanoparticles. In order to fill this novel research need in the area of improving heat transmission using NFs, an investigation has been conducted in this analysis. The originality of the existing analysis lies in examining the NF containing Ag in water-base fluid for heat enhancement and its stability over an elongating and shrinking sheet. The foremost flow equations in terms of partial differential equations (PDEs) are made dimensionless in terms of ordinary differential equations (ODEs) *via* a similar transformation. The numerical outcomes are achieved *via* a boundary-value problem fourth-order (bvp4c) scheme using MATLAB software. The impacts of emerging factors on the flowing fluid and heat rate are examined through graphs.

2 Mathematical exploration

Consider the unsteady fluid flow in a two-dimensional overstretching/shrinking sheet containing the Ag nanoparticles. The geometry of the Ag–H_2O is represented in Figure 1(a), in which the NF velocities are portrayed by and for the horizontal and vertical directions, respectively.

The basic flow equations for the considered model are [21,23]

$$\frac{\partial u}{\partial x} + \frac{\partial v}{\partial y} = 0, \tag{1}$$

$$\frac{\partial u}{\partial t} + u\frac{\partial u}{\partial x} + v\frac{\partial u}{\partial y} = \frac{\mu_{nf}}{\rho_{nf}}\left\{\frac{\partial^2 u}{\partial y^2}\right\}, \tag{2}$$

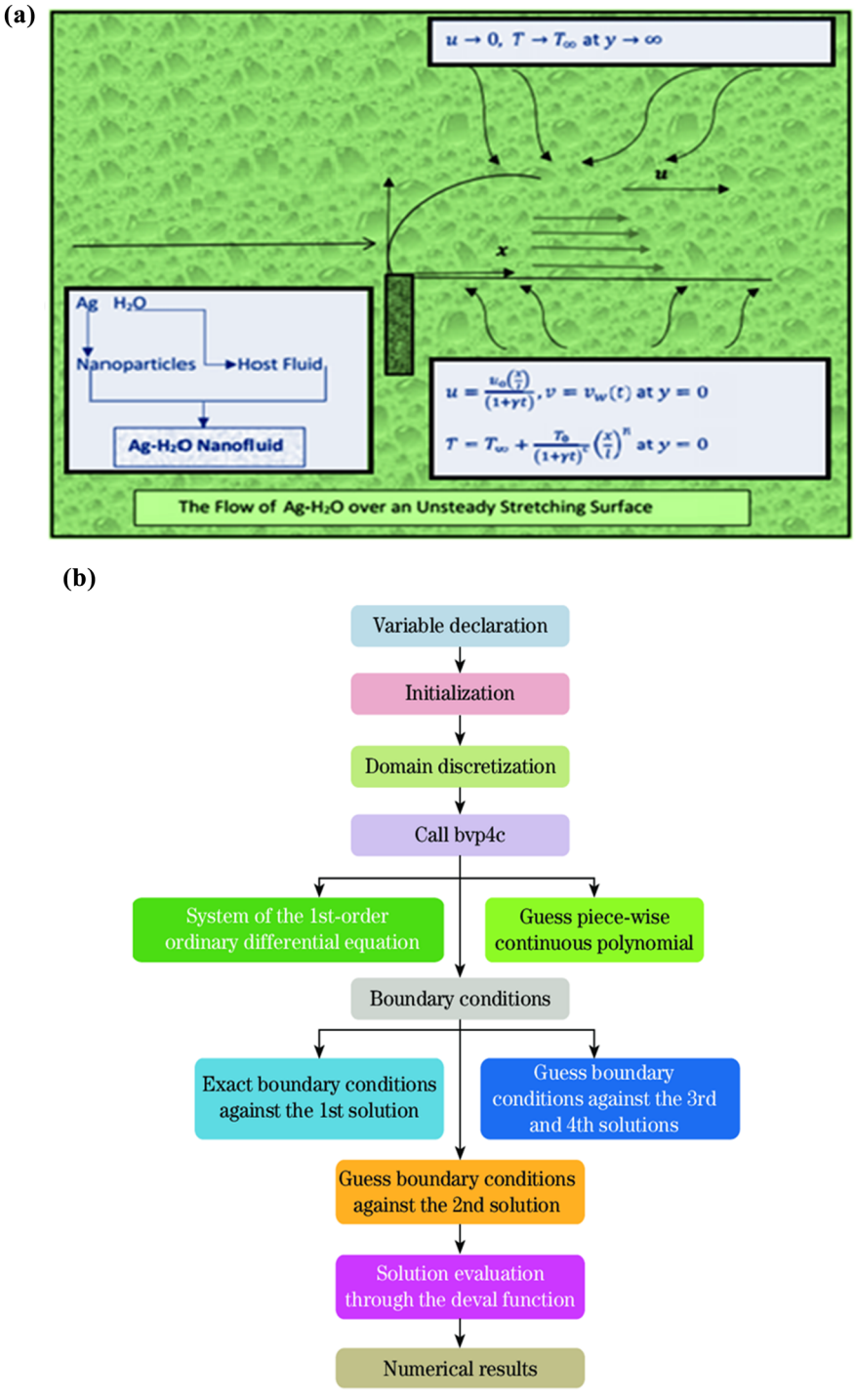

Figure 1: (a) Geometry of Ag-H_2O flow. (b) Flow chart of bvp4c.

$$\frac{\partial T}{\partial t} + u\frac{\partial T}{\partial x} + v\frac{\partial T}{\partial y} = \frac{k_{\mathrm{nf}}}{(\rho C_{\mathrm{p}})_{\mathrm{nf}}}\left(\frac{\partial^2 T}{\partial y^2}\right). \tag{3}$$

In the above equations, μ_{nf} signifies the viscosity of NF, ρ_{nf} stands for the density of NF, k_{nf} portrays the thermal conductivity of NF, and $(\rho C_{\mathrm{p}})_{\mathrm{nf}}$ describes the heat capacity of the NF. Furthermore, Table 1 represents the present model and its thermo-physical properties [21]

$$(\rho C_{\mathrm{p}})_{\mathrm{nf}} = ((1-\phi) + \phi(\rho C_{\mathrm{p}})_s(\rho C_{\mathrm{p}})_f^{-1})(\rho C_{\mathrm{p}})_f, \tag{4}$$

$$\rho_{\mathrm{nf}} = ((1-\phi) + \phi\rho_s(\rho_f)^{-1})\rho_f, \tag{5}$$

$$\mu_{\mathrm{nf}} = \mu_f(1-\phi)^{-2.5}, \tag{6}$$

$$k_{\mathrm{nf}} = k_s((k_s + 2k_f) - 2\phi(k_f - k_s))((k_s + 2k_f) + \phi(k_f - k_s))^{-1}. \tag{7}$$

The conditions at the surface and far from the surface are given below:

$$u = u_0(xl^{-1})(1+\gamma t)^{-1}, v = v_w(t), \quad T = T_\infty + T_0(1+\gamma t)^{-c}(x^n l^{-n})(\text{at the surface}), \tag{8}$$

$$u \to 0 \text{ and } T \to T_\infty \text{ (far from the surface)}. \tag{9}$$

In equations (8) and (9), the reference lengths are represented by l, n, and c, where γ, T_∞, u_0, and T_0 are positive constant.

The stream function for the present model is represented by the following equations:

$$\varphi(x,y) = xl^{-1}(\sqrt{\mathrm{Re}}\,(1+\gamma t)^{0.5})^{-1}F(\eta), \tag{10}$$

where $\mathrm{Re} = l_0(\nu_f)^{-1}$ and $\mathrm{Pr} = \frac{\nu_f}{k_f}$.

By introducing the variables of transformation for the present model [21,23], we obtain

$$\eta = \sqrt{\mathrm{Re}}\,y(l(1+\gamma t)^{0.5})^{-1}, \quad T = T_\infty + T_0(x^n l^{-n})\theta(\eta)(1+\gamma t)^{-c}, \tag{11}$$

$$u = u_0 xF'(\eta)(l(1+\gamma t))^{-1}, \tag{12}$$

$$v_w = -u_0 F(\eta)(\sqrt{\mathrm{Re}}\,(1+\gamma t)^{0.5})^{-1}. \tag{13}$$

The given flow model is a time-dependent flow problem, so we compute the atrial derivative for u and v with respect to space and t.

Using equations (12) and (13), we have

$$\frac{\partial u}{\partial x} = \frac{u_0}{l(1+\gamma t)}F'(\eta), \tag{14}$$

$$\frac{\partial u}{\partial y} = \frac{u_0 x\sqrt{\mathrm{Re}}}{l^2(1+\gamma t)^{3/2}}F''(\eta), \tag{15}$$

$$\frac{\partial^2 u}{\partial y^2} = \frac{u_0 x\,\mathrm{Re}}{l^3(1+\gamma t)^{3/2}}F'''(\eta), \tag{16}$$

$$\frac{\partial u}{\partial t} = -u_0 x\gamma(l(1+\gamma t)^2)^{-1}F'(\eta) - \frac{u_0 x\gamma y\sqrt{\mathrm{Re}}}{2l^2(1+\gamma t)^{\frac{5}{2}}}F''(\eta), \tag{17}$$

$$\frac{\partial T}{\partial t} = -T_0 c\left(\frac{x}{l}\right)^c \gamma(1+\gamma t)^{-(c+1)}\theta(\eta) - \frac{T_0\left(\frac{x}{l}\right)^c \gamma y\sqrt{\mathrm{Re}}}{2l(1+\gamma t)^{c+\frac{3}{2}}}\theta'(\eta), \tag{18}$$

$$\frac{\partial T}{\partial x} = \frac{nT_0\left(\frac{x}{l}\right)^{n-1}}{l(1+\gamma t)^c}\theta(\eta), \tag{19}$$

$$\frac{\partial T}{\partial y} = \frac{T_0\left(\frac{x}{l}\right)^c\sqrt{\mathrm{Re}}}{l(1+\gamma t)^{c+\frac{1}{2}}}\theta'(\eta), \tag{20}$$

$$\frac{\partial^2 T}{\partial y^2} = \frac{T_0\left(\frac{x}{l}\right)^c\sqrt{\mathrm{Re}}}{l^2(1+\gamma t)^{c+1}}\theta''(\eta). \tag{21}$$

In view of equations (14)–(21), the model equations described in equations (2) and (3), for the velocity and temperature profiles turned into dimensionless form as

$$F''' + \frac{(1-\phi)^{2.5}}{(1-\phi+\phi\rho_s\rho_f^{-1})^{-1}}(FF'' - F'^2 + A_1(F' + 0.5\eta F'')) = 0, \tag{22}$$

$$\theta'' + \frac{(1-\phi) + \phi(\rho C_{\mathrm{p}})_s(\rho C_{\mathrm{p}})_f^{-1}}{((k_s+2k_f) - 2\phi(k_f - k_s))((k_s+2k_f) + \phi(k_f - k_s))^{-1}}(\mathrm{Pr}A_1(c\theta + 0.5\eta\theta') + \mathrm{Pr}(n\theta F' + \theta' F)) = 0. \tag{23}$$

Here, $A_1 = \gamma l u_0^{-1}$ is the unsteadiness number, and $\mathrm{Pr} = \frac{\nu_f}{k_f}$ is the Prandtl number.

The corresponding transformed boundary conditions are

$$F(\eta_{=0}) = f_w, F'(\eta_{=0}) = 1 \text{and} F'(\eta_{=\infty}) = 0, \tag{24}$$

Table 1: Thermo-physical properties of the present model

Characteristics	Density	Heat capacity	Thermal conductivity	Electric conductivity
Silver	10,500	234	425	6.21×10^6
Water	997.1	4,179	0.613	0.005

$$\theta(\eta_{=0}) = 1 \text{ and } \theta(\eta_{=\infty}) = 0. \tag{25}$$

3 Numerical modeling of bvp4c

In MATLAB software, the bvp4c method solves the simulated highly complex differential problems (22) and (23) that align with the boundary limitations (24) and (25) numerically. This algorithm is implemented in a three-phase collocation technique, as described by Rehman *et al.* [25]. A homogeneous fourth-order resolution is implemented like solution C1-continuous in an integrated interval with the use of collocation polynomials. A mesh is implemented in the two phase using a collocation strategy to divide the time frame into sub-intervals. The algorithm ensures the assurance of the computational mechanism's response.

A solver is used to figure out the error across every subinterval. If the required tolerance is not met, the procedure is repeated with a modified mesh. Figure 1(b) shows the bvp4c workflow. First, we use the steps that follow to convert equations (18)–(21) that relate to the border conditions (23) into first-order differential problems.

Phase I: Introducing the new variables to reduce the equations (18)–(21) with corresponding condition (23) to the first order

$$\chi_1 = F, \chi_2 = F', \chi_3 = F'', \chi_4 = \theta \text{ and } \chi_5 = \theta'. \tag{26}$$

Phase II: In view of (26), equations (22)–(26) reduce to the following form:

$$\chi_1' = F', \chi_2' = F'', \chi_3' = F''', \quad \chi_4' = \theta' \text{ and } \chi_5' = \theta'', \tag{27}$$

$$\chi_3' = -\left(\frac{(1-\phi)^{2.5}}{(1-\phi+\phi\rho_s\rho_f^{-1})^{-1}}(\chi_1\chi_3 - \chi_2^2 + A_1(\chi_2 + 0.5\eta\chi_3))\right), \tag{28}$$

$$\chi_5' = -(\frac{(1-\phi)+\phi(\rho C_p)_s(\rho C_p)_f^{-1}}{((k_s+2k_f)-2\phi(k_f-k_s))((k_s+2k_f)+\phi(k_f-k_s))^{-1}} \tag{29}$$
$$(\mathrm{Pr}_1(c\chi_4 + 0.5\eta\chi_5))(\mathrm{Pr}_1(c\chi_4 + 0.5\eta\chi_5) + \mathrm{Pr}(n\chi_4\chi_2 + \chi_5\chi_1))).$$

Phase III: The altered BCs are

$$(\chi_1)_{a*} = f_w, (\chi_2)_{a*} = 1, \text{ and } (\chi_4)_{a*} = 1, \quad (\chi_2)_{b*} = 0 \text{ and } (\chi_4)_{b*} = 0. \tag{30}$$

The subscript "a*" in equation (30) indicates the surface position at $\eta = 0$, while the subscript "b*" indicates its distance to the surface at a given value of η. We have selected the range for the present investigation to be $0 \le \eta \le 7$. We establish a dual response for two distinct initial estimations by applying the bvp4c method. The initial answer is obtained by means of an initial prediction that is very ambiguous. The second branch is not always possible to achieve. Until we arrive at a solution that fulfills the boundary requirements at infinity, this iterative procedure is carried out.

4 Stability analysis

We are interested in finding the second branch for various ranges of λ in the current investigation. Finding the problem's stability assessment that is both stable and physically possible is important for this goal. The technique utilized by Merkin [17], which was recently enhanced by Weidman *et al.* [18], is also applied to the current problem.

The time-dependent flow characteristics (1)–(6) are given below:

$$\frac{\partial u}{\partial x} + \frac{\partial v}{\partial y} = 0, \tag{31}$$

$$\frac{\partial u}{\partial t} + u\frac{\partial u}{\partial x} + v\frac{\partial u}{\partial y} = \frac{\mu_{\mathrm{nf}}}{\rho_{\mathrm{nf}}}\left(\frac{\partial^2 u}{\partial y^2}\right), \tag{32}$$

$$\frac{\partial T}{\partial t} + u\frac{\partial T}{\partial x} + v\frac{\partial T}{\partial y} = \frac{k_{\mathrm{nf}}}{(\rho C_p)_{\mathrm{nf}}}\left(\frac{\partial^2 T}{\partial y^2}\right). \tag{33}$$

Following Markin [17] and Wiedman *et al.* [18], the current study uses the following similarity transformations and defines the dimensionless time variable τ as:

$$\eta = \sqrt{\mathrm{Re}}\, y(l(1+\gamma t)^{0.5})^{-1}, \quad T = T_\infty + T_0(x^n l^{-n})\theta(\eta)(1+\gamma t)^{-c}, \tag{34}$$

$$u = u_0 x F'(\eta)(l(1+\gamma t))^{-1}, \quad v_w = -u_0 F(\eta)(\sqrt{\mathrm{Re}}\,(1+\gamma t)^{0.5})^{-1}, \ \tau = \frac{ct}{1+\gamma t}. \tag{35}$$

By substituting equation (20) in equations (16)–(19), we obtain

$$\frac{\partial^3 F}{\partial \eta^3} + \frac{(1-\phi)^{2.5}}{(1-\phi+\phi\rho_s\rho_f^{-1})^{-1}}\left(F\frac{\partial^2 F}{\partial \eta^2} - \left(\frac{\partial F}{\partial \eta}\right)^2 + A_1\left(\frac{\partial F}{\partial \eta} + \frac{\eta}{2}\frac{\partial^2 F}{\partial \eta^2}\right)\right) + \frac{\partial F}{\partial \tau} = 0, \tag{36}$$

$$\frac{\partial^2\theta}{\partial\eta^2} + \frac{(1-\phi)+\phi(\rho C_p)_s(\rho C_p)_f^{-1}}{((k_s+2k_f)-2\phi(k_f-k_s))((k_s+2k_f)+\phi(k_f-k_s))^{-1}} \left(\mathrm{Pr}A_1\left(c\theta+0.5\eta\frac{\partial\theta}{\partial\eta}\right)+\mathrm{Pr}\left(n\theta\frac{\partial F}{\partial\eta}+\frac{\partial\theta}{\partial\eta}F\right)\right)+\frac{\partial\theta}{\partial\tau}=0. \quad (37)$$

The boundary conditions are

$$F(\eta,\tau)=f_w,\frac{\partial F}{\partial\eta}(\eta,\tau)=1,\theta(\eta,\tau)=1 \text{ at } \eta=0, \quad (38)$$

$$\frac{\partial F}{\partial\eta}(\eta,\tau)=0,\theta(\eta,\tau)=0,\eta\to\infty. \quad (39)$$

The stability of the system can be analyzed by perturbed it with disturbance τ, as explained by Marken [17] and Wiedman *et al.* [18]

$$F(\eta,\tau)=F_0(\eta,\tau)+\mathrm{e}^{-\gamma\tau}J(\eta,\tau),$$
$$\theta(\eta,\tau)=\theta_0(\eta,\tau)+\mathrm{e}^{-\gamma\tau}H(\eta,\tau). \quad (40)$$

In equation (40), γ represents the eigenvalues that will be determined. The stability of the problem can be analyzed using the smallest eigenvalues of γ. $F(\eta)$ and $\theta(\eta)$ are small compared to $F_0(\eta)$ and $\theta_0(\eta)$. Therefore, the disturbance $J(\eta,\tau)$, and $H(\eta,\tau)$ are small [17,18].

In view of equation (40), equations (36)–(39) become

$$J'''+\frac{(1-\phi)^{2.5}}{(1-\phi+\phi\rho_s\rho_f^{-1})^{-1}}\left(F_0J''-(J')^2+A_1\left(J'+\frac{\eta}{2}J''\right)\right) -\gamma J+\frac{\partial J}{\partial\tau}=0, \quad (41)$$

$$H''+\frac{(1-\phi)+\phi(\rho C_p)_s(\rho C_p)_f^{-1}}{((k_s+2k_f)-2\phi(k_f-k_s))((k_s+2k_f)+\phi(k_f-k_s))^{-1}} \left(\mathrm{Pr}A_1(c\theta_0+0.5\eta H')+\frac{\partial H}{\partial\tau}+\mathrm{Pr}(n\theta J'+H'F_0)\right) -\gamma H=0. \quad (42)$$

The boundary conditions are

$$F_0(\eta,\tau)=f_w,\frac{\partial J}{\partial\eta}(\eta,\tau)=1,\theta_0(\eta,\tau)=1 \text{ at } \eta=0, \quad (43)$$

$$\frac{\partial J}{\partial\eta}(\eta,\tau)=0,\theta_0(\eta,\tau)=0,\eta\to\infty. \quad (44)$$

The steady-state linear eigenvalues problem of equations (41)–(44) is given below:

Table 2: Validation of the present study

A_1	0.6	1.0	1.4
Elbashbeshy and Bazid [26]	1.3321	1.4691	1.7087
Present study	1.3310	1.4683	1.7075

$$J'''+\frac{(1-\phi)^{2.5}}{(1-\phi+\phi\rho_s\rho_f^{-1})^{-1}}\left(JJ''-(J')^2+A_1\left(J'+\frac{\eta}{2}J''\right)\right) -\gamma J=0, \quad (45)$$

$$H''+\frac{(1-\phi)+\phi(\rho C_p)_s(\rho C_p)_f^{-1}}{((k_s+2k_f)-2\phi(k_f-k_s))((k_s+2k_f)+\phi(k_f-k_s))^{-1}} (\mathrm{Pr}A_1(cH+0.5\eta H')+\mathrm{Pr}(nHJ'+H'J))-\gamma H=0, \quad (46)$$

$$J(\eta,\tau)=f_w,J'(\eta,\tau)=1,H(\eta,\tau)=1 \text{ at } \eta=0, \quad (47)$$

$$J'(\eta,\tau)=0,H(\eta,\tau)=0,\eta\to\infty. \quad (48)$$

5 Analysis and physical description

The motivation behind this study is to analyze the thermal conductivity of the NF under the effects of heat generation and absorption in a time-dependent boundary layer flow, which is an important area of research in fluid dynamics. The novelty of the existing study is that it aims to inspect the thermal characteristics of the NF for heat enhancement using Ag nanoparticles in water-base fluid across a time-dependent stretching sheet. The flow model is established for Ag–H_2O NF in terms of PDEs. The transform variables are used to obtain dimensionless flow equations in terms of ODEs and then solve *via* the bvp4c approach. For confirmation, the present study is compared with previous work, and good corresponding is established by comparing the values of the skin friction as shown in Table 2. This validation confirmed that the numerical results of the present study are definite.

Figure 2 determines the occurrences of duality, *i.e.*, the stable and unstable branches. As a consequence, a reliability analysis is performed to determine which is utmost

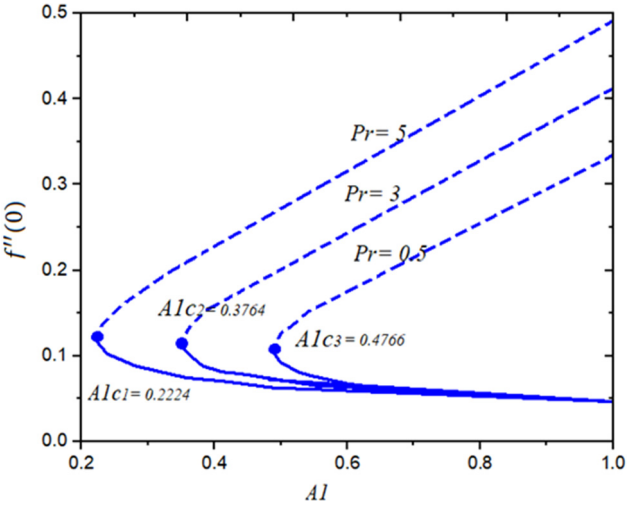

Figure 2: Smallest eigenvalues γ with suction parameter $f_w < 0$.

consistent. The linearized equations (32)–(35) are numerically solved using the bvp4c approach. Figure 2 displays the eigenvalues γ against suction parameter f_w when $A_1 = 0.5$. Here point to be noted is that the primary and second solutions are connected with the common point called the critical point. It is perceived that the first solutions (solid lines) is stable branch, whereas the second solution (dashed lines) is the unstable branch based on the previous study reported by Merkin [17] and Wiedman *et al.* [18]. The stability analysis is important and is significantly used for the stable solution when dual solutions exist, which predicts which solution is stable.

It is perceived from Table 3 that the first branch (second branch) is reliable (unstable) as the magnitude of γ is positive (negative). The positive values of γ denote the stable solution, while the negative values of γ signify the unstable solution.

Figures 3 and 4 show the variation of local skin friction $f''(0)$ regarding volume friction parameter and Prandtl number with the variation of injection factor ($f_w < 0$) and unsteadiness number A_1, respectively. From this analysis, multiple solutions have been observed for $f''(0)$. The dual solutions occur due to the injection case. Two dissimilar categories of solutions like multiple branches ($f_w \le f_{wci}$) and no branch ($f_w > f_{wci}$) for injection factor f_w exist. Furthermore, a significant change in ϕ and Pr results boost in f_{wci} and A_{1ci}, which realm a separation. It is examined that $f''(0)$ increases in both cases. In Figure 3, it is significant to point out that the critical value for $\phi = 0.01$ is $f_{wc1} = -2.007$, while the critical values for the $\phi = 0.05$ and $\phi = 0.1$ are $f_{wc2} = -2.3134$ and $f_{wc2} = -2.3134$, respectively. Similarly, the critical magnitudes for Pr = 5, 3, and 0.5 are $A_{1c1} = 0.2224$, $A_{1c2} = 0.3764$, and $A_{1c3} = 0.4766$, respectively. The behavior is observed as discussed for f_{wi}, *i.e.*, multiple branch ($A_1 \le A_{1ci}$) and no branch ($A_1 > A_{1ci}$) for A_1 exist when $f_w = -1$. It is portrayed that $f''(0)$ increases as the quantities of ϕ and Pr are enhanced. The impression of ϕ, Pr, and n on the skin friction is shown in Figures 5–7, respectively. The dual solution is observed for these parameters too. It is reported that the HT is a growing

Table 3: The eigenvalues for the numerous values of unsteadiness parameter A_1

A_1	γ	
	First branch	Second branch
−0.1	1.50778	−0.58707
−0.5	0.72587	−2.42025
−1.0	0.66487	−5.10325
−1.5	0.50010	−9.13063

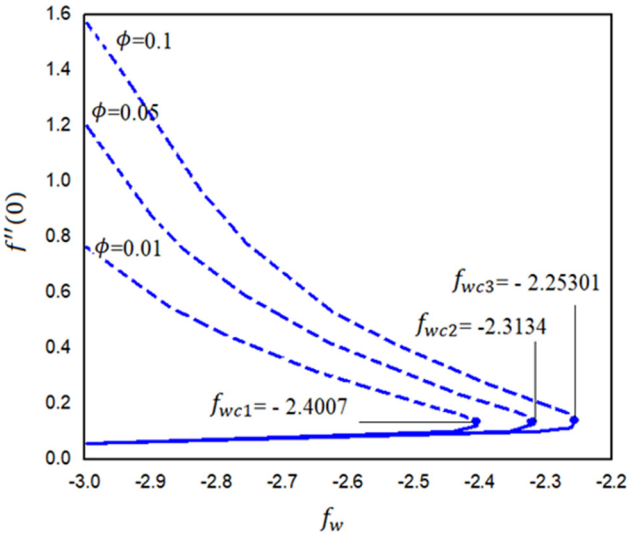

Figure 3: Variation of $f''(0)$ *via* ϕ.

function of ϕ and Pr while decreasing with the increasing values of n. The discrepancy in $f'(0)$ becomes dominant against ϕ in the first solution for a fixed value of A_1, while the setback phenomenon is observed in the second branch.

In the above figures, it is interesting to note that the foremost values of injection do not permit tension in moving molecules, and vorticity is not laminar. In the first branch, with larger injection, the decline in wall shear force as well as the rate of heat transmission is noted. In the second branch, the heat transmission is poorer, but the shear force has improved.

Figures 8–14 show the influence of emerging factors like suction/injection factor and the unsteadiness number on the dimensionless velocity and temperature of NF containing Ag nanoparticles using water-base fluid. The Pr is

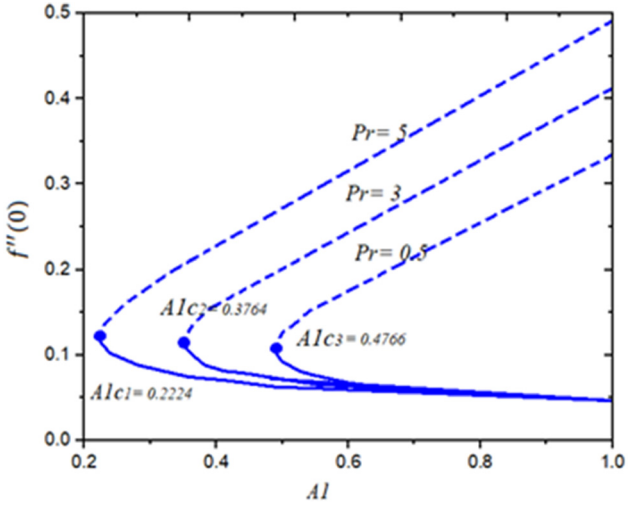

Figure 4: Disparity of $f''(0)$ *via* Pr.

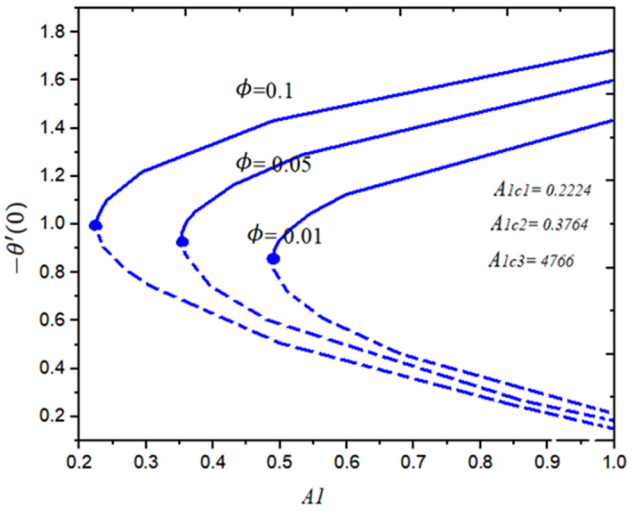

Figure 5: Disparity of $-\theta'(0)$ *via* ϕ.

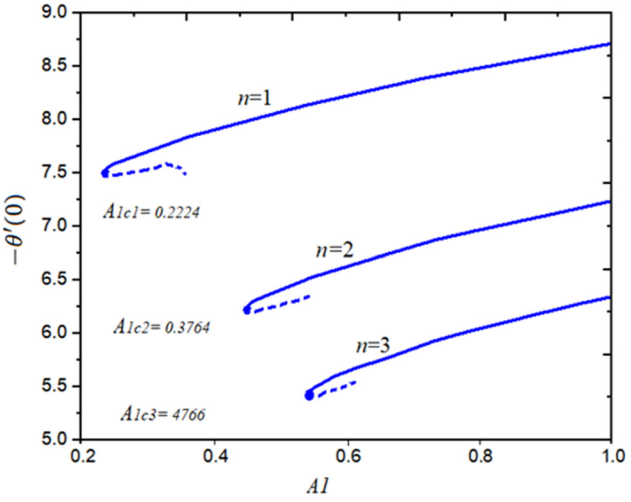

Figure 7: Variation of $-\theta'(0)$ *via* n.

taken as 6.2 as water is used as a host fluid. Figures 8 and 9 display the influence of suction and injection factors on the fluid velocity field. The impact of unsteadiness number A_1 on the velocity field is depicted in Figures 10 and 11, individually for the dissimilar values of f_w. Figures 12 and 13 show the inspiration of suction/injection and unsteadiness factor on the temperature profile. In the above analysis dual solutions has been observed for the injection case.

The influence of f_w on the velocity of the fluid is shown in Figures 8 and 9. Figure 8 shows that the fluid velocity decreases when the suction influence is increased at the sheet. From a physics point of view, when the suction is increased, more NF molecules are trapped at the sheet surface, due to which the fluid velocity declines. The dual solutions occur due to the injection $f_w = -1$. From the analysis, it is perceived that the first solution is higher (dashed lines) than the second solution (solid lines). On the other hand, the velocity of the fluid is a growing function of injection factor $f_w < 0$ as shown in Figure 9 in both cases (first and second solutions). Physically, when fluid particles leave the sheet surface due to injection, their momentum increases, which ultimately enhances the fluid motion. Additionally, the internal forces of the molecules reduce, and the thermal boundary layer thickness upsurges continuously in the first and second branches as the magnitude of injection increases.

Figures 10 and 11 depict the influence of A_1 on the NF velocity field for suction and injection, respectively. Mixed variation is examined for the velocity field both first and second solutions. It is perceived that the velocity of the fluid increases with the increasing quantities of A_1 in the

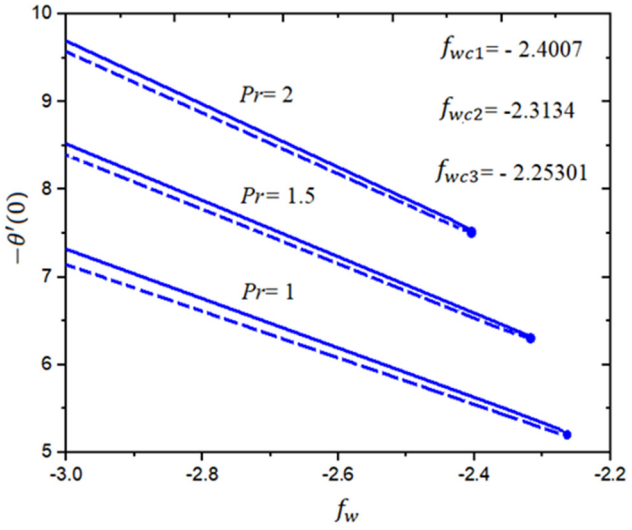

Figure 6: Variation of $-\theta'(0)$ *via* Pr.

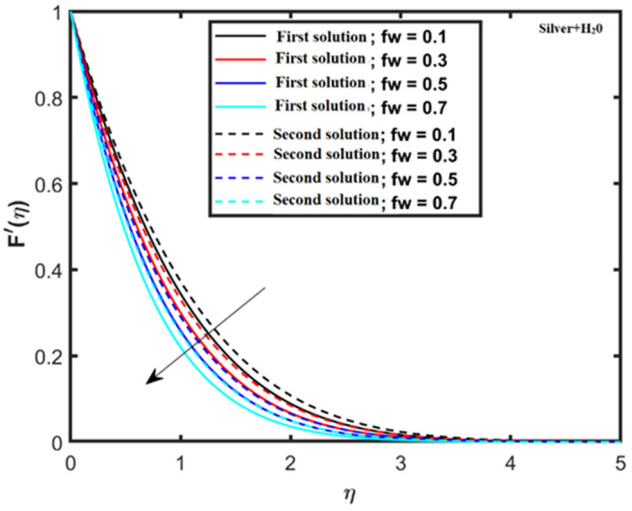

Figure 8: Velocity for suction $f_w > 0$.

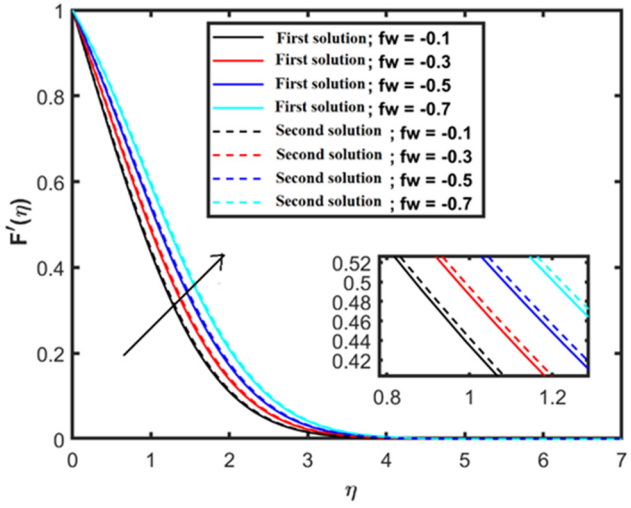

Figure 9: Velocity for injection $f_w < 0$.

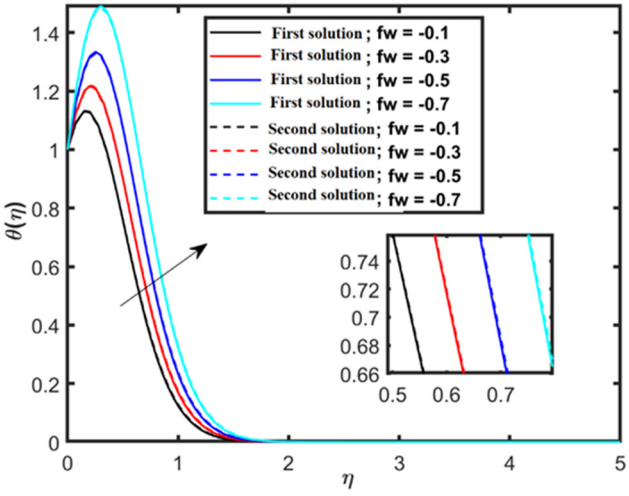

Figure 12: Temperature for injection $f_w < 0$.

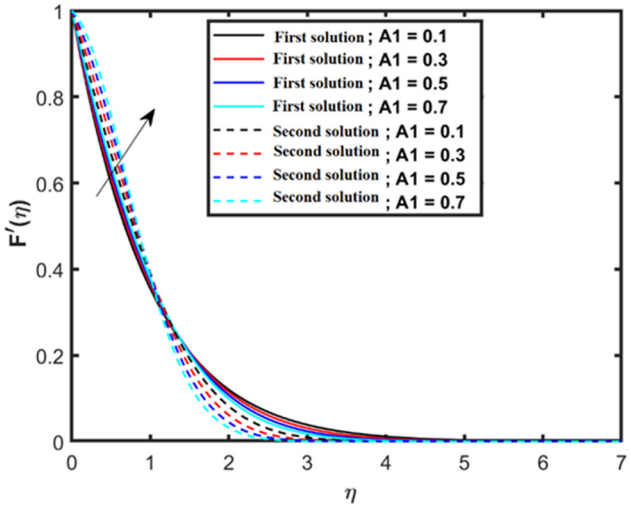

Figure 10: Velocity for suction $f_w = 1$.

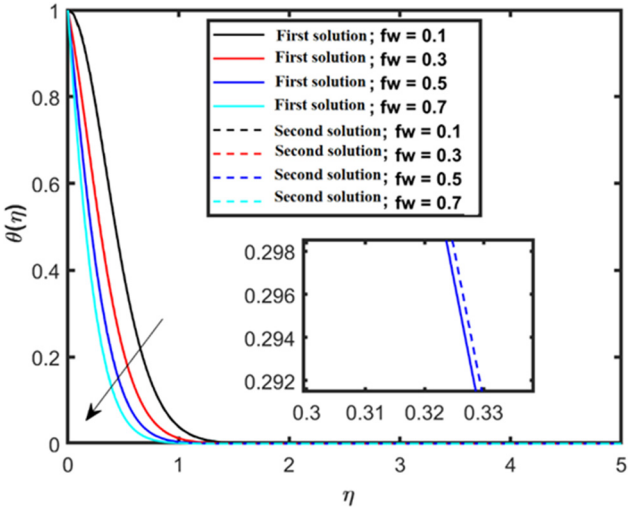

Figure 13: Temperature for suction $f_w > 0$.

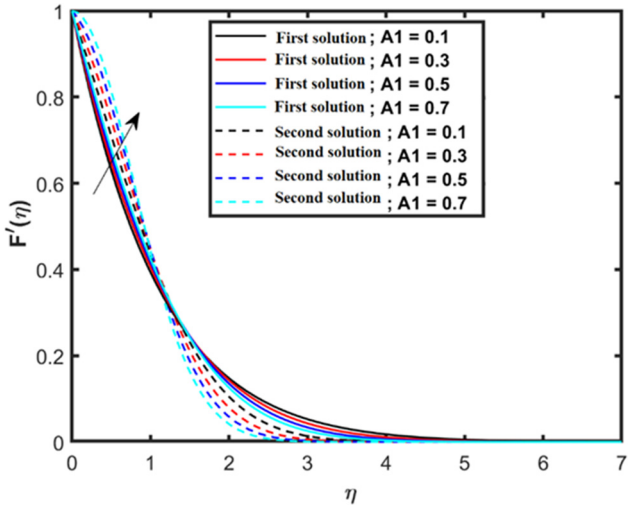

Figure 11: Velocity for suction $f_w = -1$.

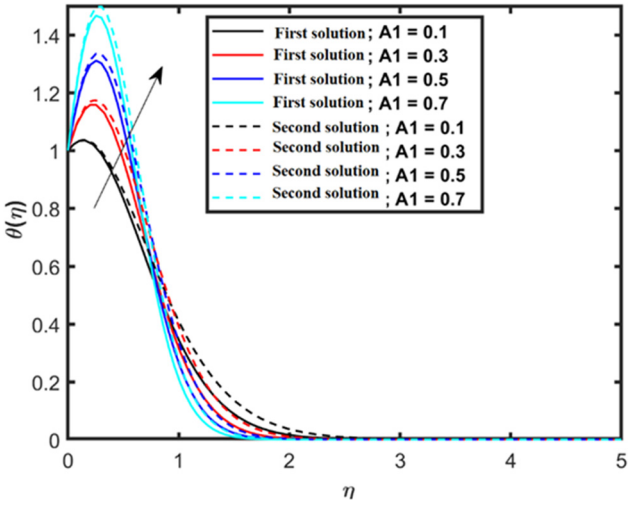

Figure 14: Temperature for suction $f_w = 1$.

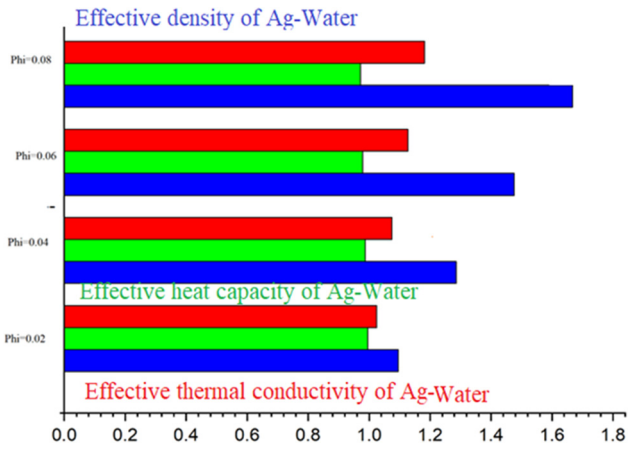

Figure 15: Effect of ϕ on thermo-physical quantities.

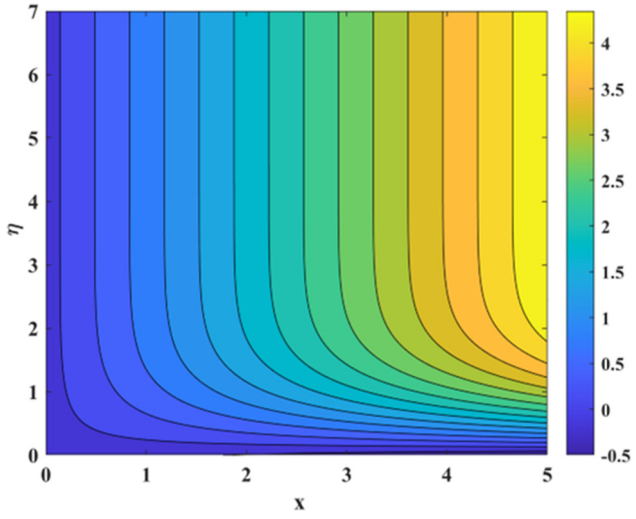

Figure 17: Streamlines for $A_1 = 1.0$.

range $0 \le \eta \le 1.5$, while the reverse effect is observed in the domain $1.5 < \eta \le 7$ which satisfy the far-field Bcs asymptotically.

Figures 12–14 show the variation of NF temperature for the suction ($f_w > 0$)/injection ($f_w < 0$) f_w and unsteadiness number A_1. Two dissimilar categories of solutions, *i.e.*, multiple branch ($f_w \le f_{wci}$) and no branch ($f_w > f_{wci}$) for injection factor f_w, exist. Similarly, multiple branch ($A_1 \le A_{1ci}$) and no branch ($A_1 > A_{1ci}$) for A_1 exist when $f_w = -1$. It is detected that the temperature regarding first and second solutions enhances for the injection case while decreases for the suction case. It is also perceived that mixture behavior is detected for the variation of the unsteadiness number. The temperature field increases in the domain $0 \le \eta \le 0.9$ and decreases in the range $0.9 < \eta \le 7$. Physically, suction causes the fluid velocity to rise quickly, increasing the dynamic energy of the fluid atoms. In elevation, kinematic energy causes a spike in particle collisions. The outcome is a dramatic rise in temperature. Due to increased injection effects close to the surface, the temperature rises quickly and vanishes asymptotically a far $\eta \ge 2$.

The volume fraction of the nanoparticles significantly affects thermophysical characteristics that are vital to the NFs' HT process. Figure 15 shows the results for active density, energetic viscosity, as well as thermal efficiency versus for the tiny fluid under study. Similarly, by increasing the volumetric percentage of the nanomaterial, efficient density and heat capacity increase.

The streamlines and thermal conductivity for the present flow study are displayed in Figures 16–19 for two different values of A_1, respectively. It is reported that the

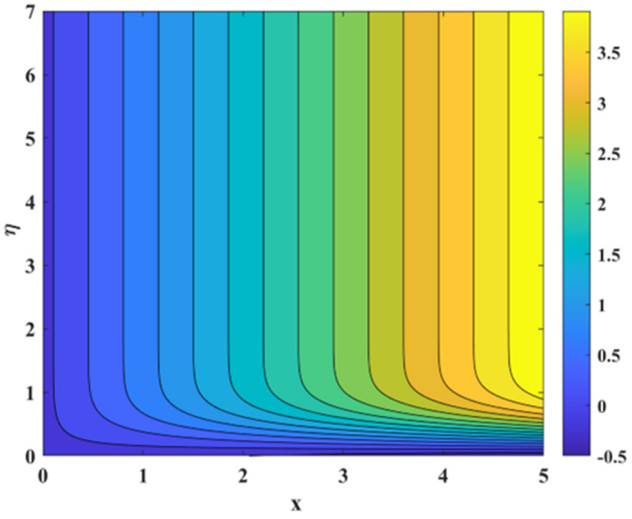

Figure 16: Streamlines for $A_1 = 0.2$.

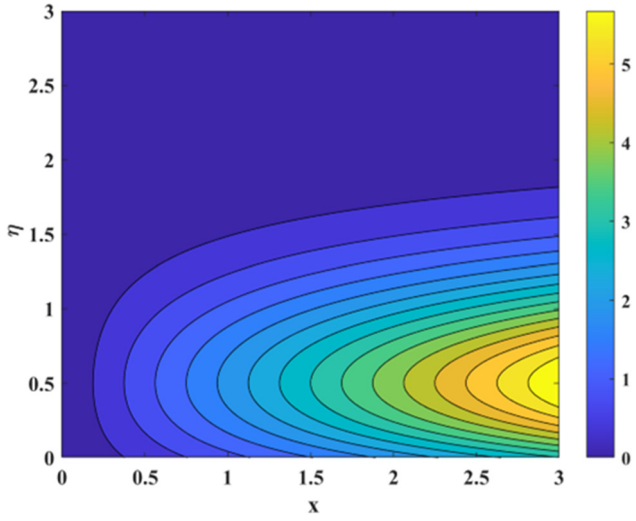

Figure 18: Thermal conductivity for $A_1 = 0.2$.

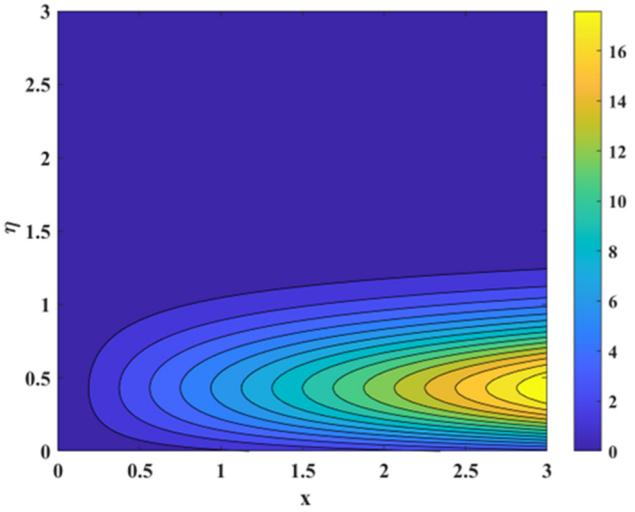

Figure 19: Thermal conductivity for $A_1 = 1.0$.

streamlines and thermal conductivity are growing function of A_1. As the quantities of A_1 are augmented from 0.2 to 1.0, a significant increasing change is observed as depicted in Figures 16 to 19, respectively.

6 Conclusions

Due to its excellent thermal performance, a new class of conventional liquids known as NFs has gained a lot of attention from scientists and engineers. As a result, a time-dependent sheet is used to organize the investigation of the thermal transport mechanism for Ag–H_2O. Such flows may be seen on the surface of bullets, solar thermal airflow, and automobile bonnets. In order to evaluate the effects of various factors on the heat transport process across a time-dependent surface, a flow issue for Ag–H_2O NF is studied. According to the investigation, the employed NF is a superior heat conductor than normal liquids, making it useful for engineering and industrial applications. Finally, a statistical assessment is offered to assess the study's reliability. It found great consistency with earlier research. Additionally, due to suction/injection phenomena, dual solutions occur for some emerging parameters. So, stability exploration is executed to ratify the stable solution. From the analysis, it is originated that the first solution is reliable, while the second is unstable. Two dissimilar categories of solutions, *i.e.*, multiple branch ($f_w \le f_{wci}$) and no branch ($f_w > f_{wci}$) for injection factor f_w, exist. Similarly, multiple branches ($A_1 \le A_{1ci}$) and no branch ($A_1 > A_{1ci}$) for A_1 exist when $f_w = -1$. A significant change in ϕ and Pr results boost in f_{wci} and A_{1ci}, which is a realm of separation. It is portrayed that $f''(0)$ increases as the quantities of ϕ and Pr are enhanced. It is reported that the HT is a growing function of ϕ and Pr while decreasing with the increasing values of n. It is reported that the fluid velocity decreases when the suction influence is increased at the sheet. The temperature field increases in the domain $0 \le \eta \le 0.9$ and decreases in the range $0.9 < \eta \le 7$. Similarly, by increasing the volumetric percentage of the nanomaterial, efficient density and heat capacity increase. Additionally, the streamlines and the thermal conductivity are increasing functions of A_1. As the magnitudes of unsteadiness number A_1 are increased from 0.2 to 1.0, a significant increasing change is observed for the streamlines and thermal conductivity.

Acknowledgments: The authors acknowledge the support by the National Research Foundation of Korea (NRF) grant funded by the Korean government (MSIT) (RS-2024-00346834).

Funding information: This work was supported by the National Research Foundation of Korea (NRF) grant funded by the Korea government (MSIT) (RS-2024-00346834).

Author contributions: All authors have accepted responsibility for the entire content of this manuscript and approved its submission.

Conflict of interest: The authors state no conflict of interest.

Data availability statement: The datasets generated and/or analyzed during the current study are available from the corresponding author on reasonable request.

References

[1] Elgazery NS. Nanofluids flow over a permeable unsteady stretching surface with non-uniform heat source/sink in the presence of inclined magnetic field. J Egypt Math Soc. 2019;27(1):1–26. doi: 10.1186/s42787-019-0002-4.

[2] Nasir S, Shah Z, Islam S, Bonyah E, Gul T. Darcy Forchheimer nanofluid thin film flow of SWCNTs and heat transfer analysis over an unsteady stretching sheet. AIP Adv. 2019;9(1):015223. doi: 10.1063/1.5083972.

[3] Raza J, Ashfaq A. Optimization of heat transfer in two-phased nanofluid flow over a biaxial sheet using Taguchi-GRA method. Multiscale Multidiscip Model Exp Des. 2025;8(1):124.

[4] Raza J, Mustafa F, Lund LA, Shah Z, Alshehri MH, Vrinceanu N. Optimization of heat transfer rate of trihybrid nanofluid embedded between two horizontal coaxial cylinders by RSM. Case Stud Therm Eng. 2024;60:104637.

[5] Shutaywi M, Raza J, Lund LA, Shah Z, Vrinceanu N, Deebani W. Optimization of heat transfer in a channel with stretching walls using a magnetized tetra-hybrid nanofluid. Adv Mech Eng. 2024;16(11):16878132241293959.
[6] Alahmadi RA, Raza J, Mushtaq T, Abdelmohsen SA, R. Gorji M, Hassan AM. Optimization of MHD flow of radiative micropolar nanofluid in a channel by RSM: sensitivity analysis. Mathematics. 2023;11(4):939.
[7] Bhattacharyya K, Layek GC. Magnetohydrodynamic boundary layer flow of nanofluid over an exponentially stretching permeable sheet. Phys Res Int. 2014;2014(1):592536. doi: 10.1155/2014/592536.
[8] Mansur S, Ishak A. Unsteady boundary layer flow of a nanofluid over a stretching/shrinking sheet with a convective boundary condition. J Egypt Math Soc. 2016;24(4):650–5.
[9] Dutta BK, Roy P. Temperature field in flow over a stretching sheet with uniform heat flux. Int Commun Heat Mass Transf. 1985;12(1):89–94.
[10] Cortell R. Viscous flow and heat transfer over a nonlinearly stretching sheet. Appl Math Comput. 2007;184(2):864–73.
[11] Afzal F, Kamran T. Advanced heat transfer analysis of 3D magnetohydrodynamic nanofluid flow over an extending sheet with thermal radiation and internal heat generation/absorption. Multiscale Multidiscip Model Exp Des. 2025;8(1):113.
[12] Mahabaleshwar US, Maranna T, Perez LM, Bognar GV, Oztop HF. An impact of radiation on laminar flow of dusty ternary nanofluid over porous stretching/shrinking sheet with mass transpiration. Results Eng. 2023;18:101227.
[13] Mahabaleshwar US, Bognár G, Baleanu D, Vishalakshi AB. Two-dimensional nanofluid due to an accelerated plate with viscosity ratio. Int J Appl Comput Math. 2022;8(3):111.
[14] Kamran T, Riaz MB, Akgul A, Ali MR. Heat transport analysis of three-dimensional magnetohydrodynamics nanofluid flow through an extending sheet with thermal radiation and heat source/sink. Results Eng. 2024;24:103262.
[15] Kamran T, Imran M, Naeem MN, Raza M. Bioconvection cross diffusion effects on MHD flow of nanofluids over three different geometries with melting. CMES-Comput Model Eng Sci. 2022;131(2):1023–39.
[16] Waqas H, Kamran T, Imran M, Muhammad T. MHD bioconvectional flow of Jeffrey nanofluid with motile microorganisms over a stretching sheet: solar radiation applications. Waves Random Complex Media. 2022;17:1–30.
[17] Merkin JH. On dual solutions occurring in mixed convection in a porous medium. J Eng Math. 1985;20:171–9.
[18] Weidman PD, Kubitschek DG, Davis AMJ. The effect of transpiration on self-similar boundary layer flow over moving surfaces. Int J Eng Sci. 2006;44:730–7.
[19] Merrill K, Beauchesne M, Previte J, Paullet J, Weidman P. Final steady flow near a stagnation point on a vertical surface in a porous medium. Int J Heat Mass Transf. 2006;49:4681–6.
[20] Harris SD, Ingham DB, Pop I. Mixed convection boundary-layer flow near the stagnation point on a vertical surface in a porous medium: brinkman model with slip. Transp Porous Media. 2009;77:267–85.
[21] Deebani W, Fadhel MA, Lund LA, Shah Z, Vrinceanu N, Shutaywi M. Investigating the interplay between duality and stability in magnetized radiative mixed convection of Casson nanofluid flow over a stretching/shrinking cylinder. J Radiat Res Appl Sci. 2025;18(1):101267.
[22] Asghar A, Dero S, Lund LA, Shah Z, Alshehri MH, Vrinceanu N. Slip effects on magnetized radiatively hybridized ferrofluid flow with acute magnetic force over shrinking/stretching surface. Open Phys. 2024;22(1):20240052.
[23] Yashkun U, Lund LA, Zaimi K, Shah Z, Alshehri MH, Vrinceanu N, et al. Computational study of magnetite-ethylene glycol–water-based hybrid nanofluid dynamics on an exponential shrinking/stretching Riga surface under radiative heat flux. Colloid Polym Sci. 2025;303(1):95–109.
[24] Soomro AM, Fadhel MA, Lund LA, Shah Z, Alshehri MH, Vrinceanu N. Dual solutions of magnetized radiative flow of Casson Nanofluid over a stretching/shrinking cylinder: Stability analysis. Heliyon. 2024;10(8):1–16.
[25] Rehman KU, Qaiser A, Malik MY, Ali U. Numerical communication for MHD thermally stratified dual convection flow of Casson fluid yields by stretching cylinder. Chin J Phys. 2017;55(4):1605–14.
[26] Elbashbeshy EMA, Bazid MAA. Heat transfer over an unsteady stretching surface. Heat Mass Transf. 2004;41:1–4.